Can Neural Nets Learn the Same Model Twice? Investigating Reproducibility and Double Descent from the Decision Boundary Perspective

Gowthami Somepalli [1], Liam Fowl [1], Arpit Bansal [1], Ping Yeh-Chiang [1], Yehuda Dar [2], Richard Baraniuk [2], Micah Goldblum [3], Tom Goldstein [1]

[1] University of Maryland, College Park
{gowthami, pchiang, tomg}@cs.umd.edu
lfowl@math.umd.edu, bansal01@umd.edu

[2] Rice University
{ydar, richb}@rice.edu

[3] New York University
goldblum@nyu.edu

Abstract

We discuss methods for visualizing neural network decision boundaries and decision regions. We use these visualizations to investigate issues related to reproducibility and generalization in neural network training. We observe that changes in model architecture (and its associate inductive bias) cause visible changes in decision boundaries, while multiple runs with the same architecture yield results with strong similarities, especially in the case of wide architectures. We also use decision boundary methods to visualize double descent phenomena. We see that decision boundary reproducibility depends strongly on model width. Near the threshold of interpolation, neural network decision boundaries become fragmented into many small decision regions, and these regions are non-reproducible. Meanwhile, very narrows and very wide networks have high levels of reproducibility in their decision boundaries with relatively few decision regions. We discuss how our observations relate to the theory of double descent phenomena in convex models. Code is available at https://github.com/somepago/dbViz.

1. Introduction

The superiority of neural networks over classical linear classifiers stems from their ability to slice image space into complex class regions. While neural network training is certainly not well understood, existing theories of neural network training mostly focus on understanding the geometry of loss landscapes [5, 8, 25]. Meanwhile, considerably less is known about the geometry of class boundaries. The geometry of these regions depends strongly on the inductive bias of neural network models, which we do not currently have tools to rigorously analyze. To make things worse, the inductive bias of neural networks is impacted by the choice of architecture, which further complicates theoretical analysis.

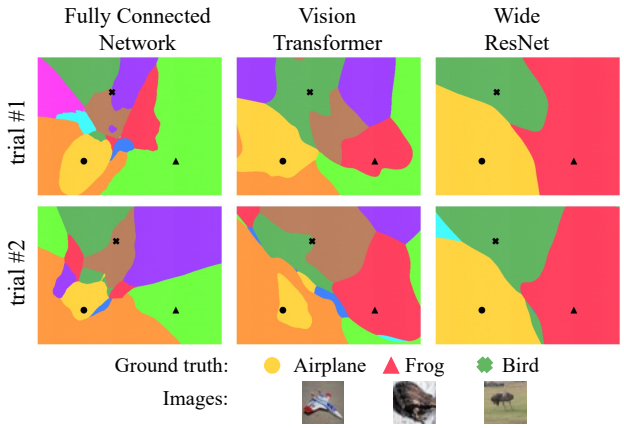

Figure 1. The class boundaries of three architectures, plotted on the plane spanning three randomly selected images. Each model is trained twice with random seeds. Decision boundaries are structurally similar across runs of the same model, and there are consistent structural difference between the class regions of different architectures.

In this study, we use empirical tools to study the geometry of class regions, and how neural architecture impacts inductive bias. We do this using visualizations and quantitative metrics calculated using realistic models. We start by presenting simple methods for decision boundary visualization. Using visualization as a tool, we do a deep dive on three main issues:

- Do neural networks produce decision boundaries that are consistent across random initializations? Put simply, can a neural network learn the same model twice? We see empirically that the decision boundaries of a network have strong similarities across runs, and we

confirm this using quantitative measurements.

- Do different neural architectures have measurable differences in inductive bias? Indeed, we find clear visible differences between the class regions of different model architectures (e.g., ResNet-18 vs ViT).
- We use decision boundary visualizations to investigate the "double descent" phenomenon. We see that decision boundaries become highly unstable and fragmented when model capacity is near the interpolation threshold, and we explore how double descent in neural networks relates to known theory for linear models.

2. Plotting decision boundaries

Most prior work on decision boundary visualization is for the purpose of seeing the narrow margins in adversarial directions [18, 21]. Fawzi et al. [11] visualize the topological connectivity of classification regions. To facilitate our studies, we seek a general-purpose visualization method that is simple, controllable, and captures import parts of decision space that lie near the data manifold.

2.1. On-manifold vs off-manifold behavior

When plotting decision boundaries, it is important to choose a method that captures the behavior of models near the data manifold. To understand why, consider the plots of decision boundaries through planes spanning randomly chosen points in input space as shown in Fig. 2. We see that decision regions are extremely smooth and uniform with few interesting features. The training process, which structures decision boundaries near the data manifold (e.g. Fig. 1), fails to produce strong structural effects far from the manifold (e.g. Fig. 2).

The uniform off-manifold behavior is not particular to our training method or architecture but is rather an inevitable consequence of the concentration of measures phenomenon [24, 31]. In fact, we can show that any neural network that varies smoothly as a function of its input will assume nearly constant outputs over most of input space. The proof of the following result is in Appendix A.

Lemma 2.1 *Let $f : [0,1]^n \to [0,1]$ be a neural network satisfying $|f(x) - f(y)| \leq \frac{L}{\sqrt{n}}\|x - y\|$. Let $\bar{f}$ denote the median value of f on the unit hypercube. Then, for an image $x \in [0,1]^n$ of uniform random pixels, we have $|f(x) - \bar{f}| \leq t$ with probability at least*

$$1 - \frac{Le^{-2\pi n t^2/L^2}}{\pi t\sqrt{n}}.$$

2.2. Capturing on-manifold behavior

The lemma above shows the importance of capturing the behavior of neural networks near the data manifold. Unfortunately, the structure of image distributions is highly complex and difficult to model. Rather than try to identify and flatten the complex structures on which images lie, we take an approach that is inspired by the recent success of the highly popular paper on the mixup regularizer [40], which observed that, in addition to possessing structure near the data manifold, *decision boundaries are also structured in the convex hull between pairs of data points*.

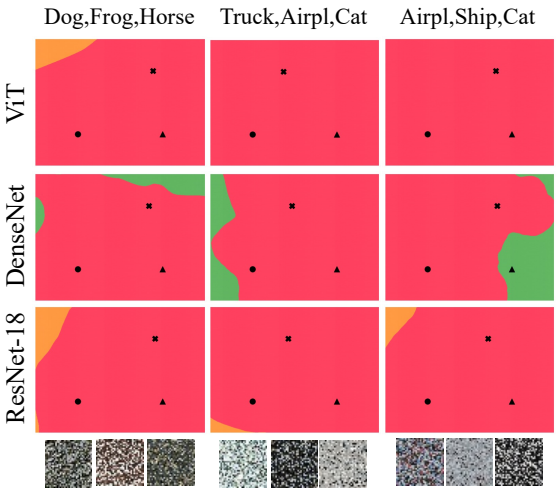

Figure 2. Off-manifold decision boundaries near "random" images created by shuffling pixels in CIFAR-10 images. Each column's title shows the labels of the unshuffled base images. Below each column we show the shuffled image triplet. Color-class mapping is as follow Red:Frog, Green:Bird, Orange:Automobile.

We take a page from the mixup playbook and plot decision boundaries along the convex hull between data samples. We first sample a triplet $(x_1, x_2, x_3) \sim \mathcal{D}^3$ of i.i.d. images from the distribution $\mathcal{D}$. Then, we construct the plane spanned by the vectors $\vec{v_1} = x_2 - x_1$, $\vec{v_2} = x_3 - x_1$ and plot the decision boundaries in this plane. To be precise, we sample inputs to the network with coordinates

$$\alpha \cdot \max(\vec{v_1} \cdot \vec{v_1}, |\text{proj}_{\vec{v_1}} \vec{v_2} \cdot \vec{v_1}|)\vec{v_1} + \beta(\vec{v_2} - \text{proj}_{\vec{v_1}} \vec{v_2})$$

for $-0.1 \leq \alpha, \beta \leq 1.1$. This plotting methods using planes has several advantages. It shows the regions surrounding multiple data points at once and also the decision boundaries between their respective classes, using just one plot. Furthermore, these classes can be chosen by the user. It also focuses on the convex hull between points rather than random directions that may point away from the manifold.

Fig. 1 shows decision regions plotted along the plane spanned by three data points chosen at random from the *Airplane*, *Frog*, and *Bird* classes of CIFAR-10 [23]. In these plots, each color represents a class label. Same color-class schema is maintained through out the paper and can be seen in legends of multiple plots.

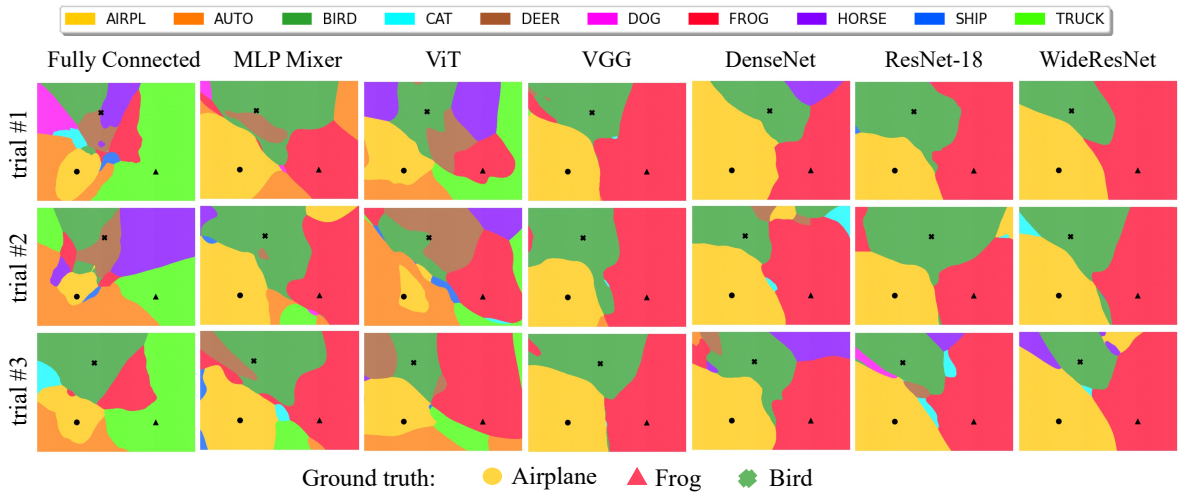

Figure 3. Decision regions through a triplet of images, for various architectures (columns) and initialization seeds (rows).

2.3. Experimental Setup:

Architectures used: We select several well-known networks from diverse architecture families[1]. We consider a simple Fully Connected Network with 5 hidden layers and ReLU non-linearities, DenseNet-121 [20], ResNet-18 [17], WideResNet-28x10, WideResNet-28x20, WideResNet-28x30 [38], ViT [9], MLPMixer [35], and VGG-19 [32]. For fast training, our ViT has only 6 layers, 8 heads, and patchsize 4. The custom MLPMixer we use has 12 hidden layers with hidden embedding dimension 512 and patch size 4. Unless otherwise stated, architectures are trained for 100 epochs using SGD optimizer, and 3 multi-step learning rate drops. Random Crop and Horizontal Flip data augmentations are used in training. For distillation experiments, we also use a ViT-S/16 pretrained on ImageNet [7] as a teacher [36]. Some experiments use the Sharpness-Aware Minimization (SAM) optimizer [12] adversarial radius set to $\rho = 0.01$.

We select learning rates using a grid search across $\{0.001, 0.002, 0.005, 0.01, 0.02, 0.05\}$ for each architecture and optimizer (Adam [22] and SGD) combination, and training for 200 epochs. Mean test accuracy over 3 runs per model is reported in Table 1.

3. Model reproducibility and inductive bias

It is known that neural networks can easily overfit complex datasets, and can even interpolate randomly labeled images [39]. Despite this flexibility, networks have an important *inductive bias* – they have a strong tendency to converge on decision boundaries that generalize well. Our goal in this section is to display the inductive bias phenomenon using decision boundary visualizations. We ask two questions:

- Can a model replicate the same decision boundaries twice, given different random initializations?
- Are there disparities between the inductive biases of different model families that result in different decision boundaries?

Below, we consider various sources of inductive bias, including neural architecture family, network width, and the choice of optimizer.

3.1. Inductive bias depends on model class

We choose three random images from the CIFAR-10 training set, construct the associated plane through input space, and plot the decision regions for 7 different architectures in Fig. 3. For each model, we run the training script three times with different random initializations.

Several interesting trends emerge in this visualization. First, we observe systematic differences between model families. Convolutional models all share similar decision boundaries, while the boundaries of Fully Connected Nets, ViT, and MLP Mixer share noticeable differences. For example, ViT and MLP Mixer consistently show the presence of an orange "Automobile" region that CNNs do not. Fully Connected Nets show considerably more complex and fragmented decision regions than other model families.

At the same time, we observe strong reproducibility trends across runs with different random seeds. This trend is particularly high for convolutional architectures, and the effect is quite strong for WideResNet, which leads us to hypothesize that there may a link between model width and reproducibility – an issue that we will investigate in more detail below.

[1]Architecture implementations from https://github.com/kuangliu/pytorch-cifar and https://github.com/lucidrains/vit-pytorch

3.2. Quantitative analysis of decision regions

The visualizations in Fig. 3 suggest that reproducibility is high within a model class, while differences in inductive bias result in low similarities across model families. To validate our intuitions, we use quantitative metrics derived from the decision plots averaged over many trials to provide a more sensitive and conclusive analysis.

Region Similarity Score: We define a metric of similarity between the decision regions of pairs of models. We first sample triplets $T_i = (x_0, x_1, x_2)_i$ of i.i.d. images from the training distribution. Let S_i be the set of points in the plane defined by T_i at which the decision regions are evaluated. We define the region similarity score:

$$R(\theta_1, \theta_2) = \mathbb{E}_{T_i \sim \mathcal{D}} \left[(|f(S_i, \theta_1) \cap f(S_i, \theta_2)|)/|S_i| \right] \quad (1)$$

where for notation simplicity we denote the set of class predictions within each decision region as $f(S_i, \theta) = \{(x, f(x; \theta))\}_{x \in S_i}$ for a model with parameters θ. Practically, we estimate the expectation in Eq. (1) by sampling 500 triplets and 2500 points in each truncated plane for a total of $1.25M$ forward passes. Simply put, this corresponds to the "intersection over union" score for two decision boundary plots.

This score can quantify similarity of decision regions across architectures, initializations, minibatch ordering, etc. When computed for a given architecture, region similarity score reflects the reproducibility of decision regions. In earlier work [3], variability of the decision boundaries is studied by examining the similarity of predictions at test points. In contrast, our method gives a much richer picture of the variance of the classification regions not just at the input points, but also in the regions around them and can be applied to both train and test data.

Measuring architecture-dependent bias We apply the region similarity score to measure decision region consistency between different training runs with the same architecture and across different architectures. For each model pair, we compute the region similarity score across 5 different training runs and 500 local decision regions, each containing 2,500 sampled points (6.25M total forward passes compared).

Fig. 4 shows region similarity scores for various architectures, and we see that quantitative results strongly reflect the trends observed in the decision regions of Fig. 3. In particular, it becomes clear that

- The inductive biases of all the convolutional architectures are highly similar. Meanwhile, MLPMixer, ViT and FC models have substantially different decision regions from convolutional models and from each other.

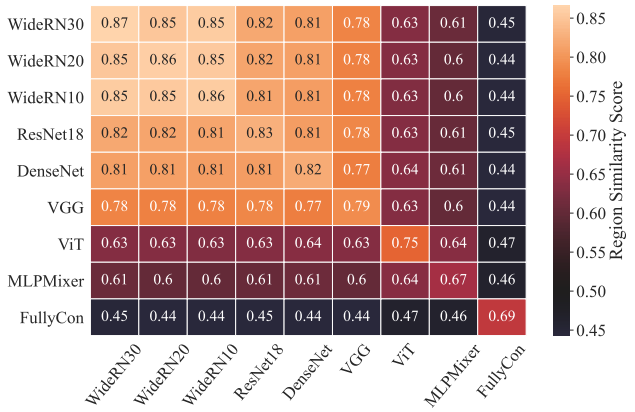

Figure 4. Region similarity scores across several popular architectures. Diagonal scores reflect the reproducibility of the models.

- Wider convolutional models appear to have higher reproducibility in their decision regions, with WideRN30 being both the widest and most reproducible model in this study.
- Skip connections have little impact on the shape of decision regions. ResNet (with residual connections across blocks), DenseNet (with many convolutional connections within blocks), and VGG (no skip connections) all share very similar decision regions. However it is worth noting that skip connection architectures achieve slightly higher region similarity scores than the very wide VGG network.

3.3. Does distillation preserve decision boundaries?

Distillation [19] involves training a student model on the outputs of an already trained teacher model. Some believe that distillation does indeed convey information about the teacher's decision boundary to the student [15], while others argue distillation improves generalization through other mechanisms [34]. We calculate the relative similarity of the student's decision boundary to its teacher's boundary and compare this to the similarity between teacher network and a network of the student's architecture and initialization but trained in a standard fashion. Across the board, distilled students exhibit noticeably higher similarity to their teachers compared with their vanilla trained counterparts. In Fig. 5, we see that *almost every* student-teacher combination has a higher region similarity score than the same teacher compared to an identically initialized model trained without distillation.

3.4. The effect of the optimizer

In addition to the influence of initialization, data ordering, and architecture, the choice of optimizer/regularizer used during training can greatly impact the resulting model [13]. Thus, we study the effect of optimizer choice on

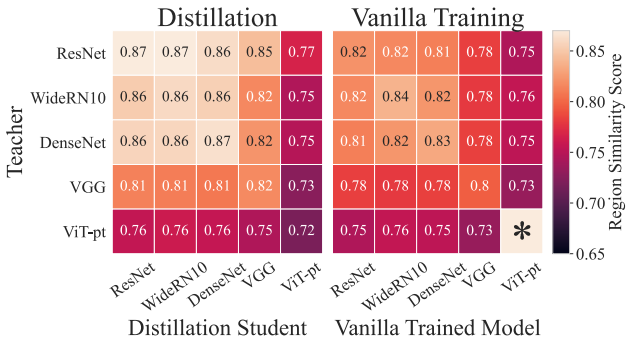

Figure 5. Region similarity scores between teacher models and distilled students and vanilla trained models. *The score is not applicable for this diagonal entry because we start from the same pre-trained model.

Region Similarity Scores

	Adam	SGD	SGD + SAM
ResNet-18	79.81	83.74	**87.22**
VGG	81.19	80.92	**84.21**
MLPMixer	67.80	66.51	**68.06**
VIT	69.55	75.13	**75.19**

Test Accuracy

	Adam	SGD	SGD + SAM
ResNet-18	93.04	95.30	**95.68**
VGG	92.87	93.13	**93.90**
MLPMixer	**82.22**	82.04	82.18
VIT	70.89	**75.49**	74.72

Table 1. Region similarity scores of models when using different optimizers for a given architecture. SGD produces more reproducible decision boundaries relative to Adam, and SGD+SAM almost always consistently increase reproducibility of the model relative to SGD.

the reproducibility of a network's decision boundary. In Table 1, we can see that SAM [12] induces more reproducible decision boundaries than standard optimizers such as SGD and Adam. This observation suggests that SAM has a stronger regularization effect. However, more regularization doesn't always mean better test accuracy. For example, for MLPMixer and ViT, using SAM does not always achieve the highest test accuracy but does achieve the highest region similarity score.

4. Double descent

In classical learning theory, it is thought that models with too few parameters (e.g., low width) generalize poorly because they are not expressive enough to fit the data, while models with too many parameters generalize poorly because of over-fitting. This is known as the Bias-Variance trade-off [14]. In contrast, the strong inductive bias of neural networks enables them to achieve good performance even with extremely large numbers of parameters. Belkin et al. [4] and Nakkiran et al. [27] have shown that under the right training conditions, we can see neural models operating in both the classical and over-parameterized regimes. This is depicted in Fig. 6, which plots test error as a function of model width on CIFAR-10. We observe a classic U-shaped curve for widths less than 10 (the underparametrized regime). For models of width greater than 10, the test error fall asymptotically (overparametrized regime). This behaviour is referred to as "double descent" and discussed in generality in Belkin et al. [4]. Between the two regimes is a model that lives at the "interpolation threshold"; here, the model has too many parameters to benefit from classical simplicity bias, but too few parameters to be regularized by the inductive bias of the over-parameterized regime. Double descent has been studied rigorously for several simple and classical model families, including kernel methods, linear models, and simple MLPs [2, 6, 16, 26, 29, 30, 33]. Double descent is now well described for linear models and random feature networks in [1, 6, 10, 16]. In the classical regime, bias decreases with increased model complexity, while the variance increases at the same time, resulting in a U-shaped curve. Then, in the overparameterized regime, the variance decreases rapidly while bias remains low [28, 37]. In our studies above, we visualized the over-parameterized regime and saw that models become highly reproducible, with wide architectures producing nearly identical models across training runs. These visualizations captured the low-variance of the over-parameterized regime.

In this section, our goal is to gain insight into the model behaviors that emerge at the interpolation threshold, causing double descent. We observe closely what is happening at critical points (i.e., the transition between the under and overparameterized regimes), and how the class boundaries transition as we increase the capacity of the model class. We find that the behaviour of class boundaries aligns with the bias-variance decomposition findings of [28, 37], however the model instabilities that cause variance to spike in neural networks is manifested as a complex fragmentation of decision space that is not, to the best of our knowledge, described in the literature on classical models.

Experimental setup: We follow the experimental setting from Nakkiran et al. [27] to replicate the double descent phenomenon for ResNet-18 [17]. We increase model capacity by varying the number of filters in the convolutional layers by a "width" parameter, k. Note that a standard ResNet-18 model has $k = 64$ and lives in the over-parameterized regime on CIFAR-10. We train models with cross-entropy loss and the Adam optimizer with learning-rate 0.0001 for

Figure 6. Test error curves with 0 and 20% label noise in training.

4000 epochs. This gentle but long training regiment ensures stability and convergence for the wide range of models needed for this study.

It was observed in [27] that label noise is important for creating easily observable double descent in realistic models. We train two sets of models, one with a clean training set and another with 20% label noise (uniform random incorrect class labels). In both cases, we use the standard (clean) test set. For noisy experiments, the same label errors are used across epochs and experiments. RandomCrop and RandomHorizontalFlip augmentations are used while training. We observe a pronounced double-descent when label noise is present. See Fig. 6, which replicates the double-descent curve of Nakkiran et al. [27].

We focus on several important model widths: $k = 4$ is the local minimum of test error in the underparametrized regime, and $k = 10$ achieves peak error ($\approx$ interpolation threshold) beyond which the test error will continually fall. We refer the reader to Appendix D for training error plots showing the onset of interpolation near $k = 10$.

4.1. How do decision boundaries change as we cross the interpolation threshold?

In Fig. 7, we plot decision boundaries for models trained with and without label noise and with varying capacities. As we move from left to right in the figure, model capacity sweeps from $k = 1$ (under-parameterized) to $k = 64$ (standard ResNet-18, which is over-parameterized). As above, visualizations take place in the plane spanned by three data points. We present examples using two different methods for sampling – one with all three images from the same class and one with three different classes. In both cases all three images are drawn from the training set and are correctly labeled (even for the experiments involving label noise). Similar behaviours are observed for other randomly sampled images and with other combinations of classes. See Appendix D for additional examples.

The mechanism behind the error spike in the double descent curve is captured by the visualizations using label noise. In this case, the under-fitting behavior of the classical regime is apparent at $k = 4$, as the model fits only 1 out of 3 points correctly. When we reached $k = 10$ (the interpolation threshold), the model fits most of the training data, including the three points in the visualization plane. As we cross this threshold, the decision regions become chaotic and fragmented. By the time we reach $k = 20$, the fragmentation is reduced and class boundaries become smooth as we enter the over-parameterized regime.

To refine our picture of double descent, we visualize the class boundaries at $k = 10$ for a range of different image triplets in Appendix Fig. 14, both with and without label noise. We see that in the label noise case, where double descent is observed, there is a clear instability in the classification behavior at the interpolation threshold.

Let's now see what happens to the decision boundaries around mislabeled images. Fig. 8 shows decision boundaries around three points from the *Automobile* class, where one of the points is mislabeled in the training set. When $k = 10$, we see chaotic boundaries. The mislabeled points are assigned their (incorrect) dataset label, but they are just barely interpolated in the sense that they lie very near the decision boundary. For $k = 64$, the boundaries are seemingly regularized by inductive bias; the mislabeled points lie in the center of their respective regions, and boundaries are much more smooth.

Having observed the qualitative behaviour of correctly labeled and mislabeled points in models with and without label noise at various capacities, we ask the following questions:

- Can quantitative methods validate that fragmentation behavior persists across multiple decision regions at the interpolation threshold and vanishes elsewhere?
- Is the fragmentation at the interpolation threshold indeed caused by model variance? In other words, do we observe different decision boundaries across training runs, or are the chaotic regions reproducible like the regions we observed in the over-parameterized regime?
- What is the mechanism for the decrease in test error in the wide model regime? Is it caused by shrinkage of the misclassified regions around mislabeled points, causing them to stop contaminating the test accuracy? Or is it merely caused by the vanishing of unnecessary fragmentation behavior for large k?

In the subsequent sub-sections, we investigate these issues using quantitative measurements of decision regions.

4.2. Quantifying fragmentation

We have observed that decision regions appear to become highly fragmented as we cross the interpolation threshold. To verify that our results are repeatable across many experiments and triples, we introduce the *fragmentation score*, which counts the number of connected class regions in the plane spanned by a triplet of images.

Let S_i be a local classification region spanned by a triplet T_i. We create a decomposition $S_i(\theta) = \cup_{j=1}^{n_i} P_j(\theta)$ where

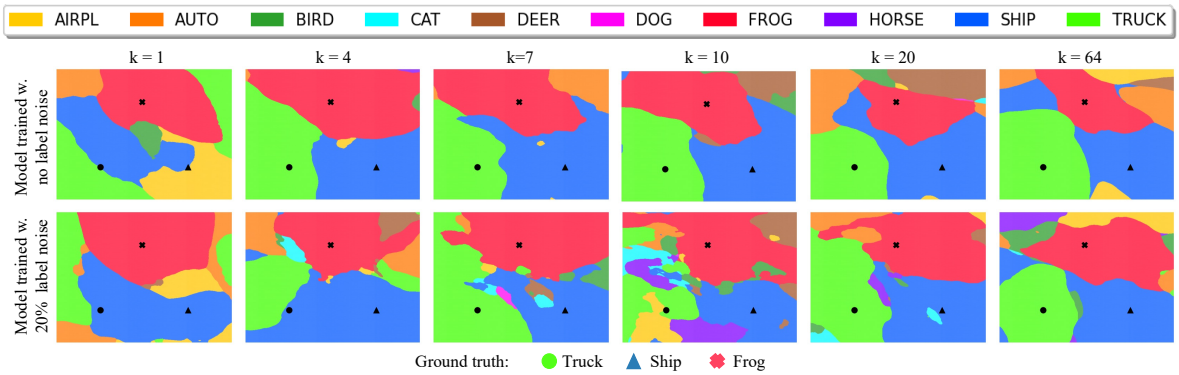

(a) All the points in the triple are from different classes, and are correctly labeled in the train set (even in the label noise case).

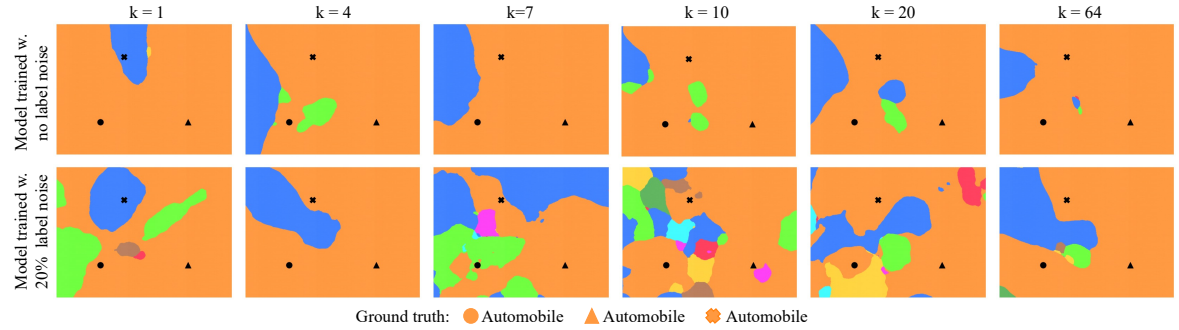

(b) All points in the triple are from the same class, Automobile, and are correctly labeled in the train set (even in the label noise case).

Figure 7. **Decision boundaries for models of varying width.** Label noise induces chaotic fragmentation of decision regions as we cross the threshold of interpolation ($k = 10$), while very narrow and wide models remain smooth. Note that $k = 10$ does not necessarily be threshold of interpolation for no label noise scenario. We see later that $k = 7$ as a potential candidate for this case.

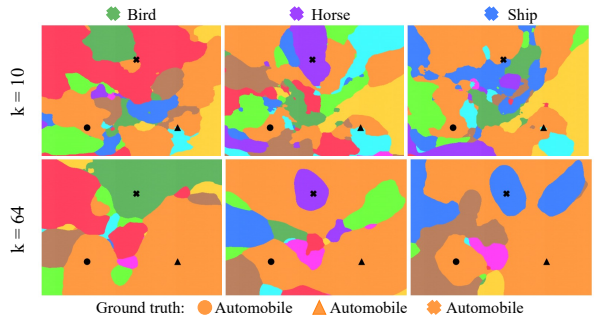

Figure 8. Decision boundaries with 1 mislabeled automobile and 2 correctly labeled automobiles. Each column represents a different image triplet. The mislabeled point is marked by x.

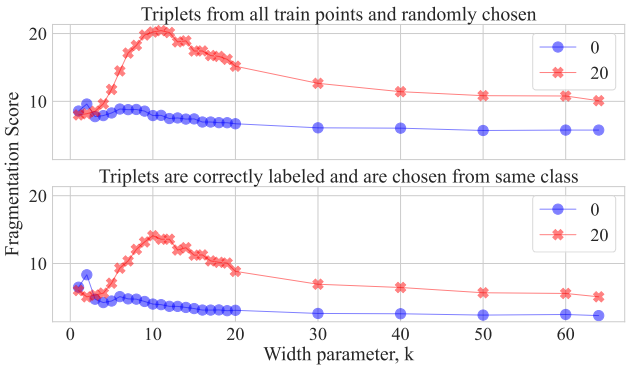

Figure 9. Fragmentation scores as a function of model width for models trained with and without label noise.

each $P_j(\theta)$ is a disjoint, maximal, path-connected component corresponding to a *single* predicted class label for the model with parameters θ. The fragmentation score $F(\theta, T_i)$ of model θ within the decision region defined by T_i is then the number of path-connected regions. The overall fragmentation score for a model is

$$F(\theta) = \mathbb{E}_{T_i \sim \mathcal{D}} F(\theta, T_i). \quad (2)$$

In practice, we compute the fragmentation score of a model using a watershed method to find connected regions in decision region spanned by the triplet and then by averaging such fragmentation counts over 1000 triplets.

Note that prior work [11] proposes a metric to understand class connectivity that requires solving a non-convex optimization problem to find an explicit path between any two given points. In contrast, our fragmentation score is scalable, does not require any backward passes to approximate the complexity of decision boundaries, and can be averaged over a large number of input triples.

Fragmentation scores as a function of model width are depicted in Fig. 9. With label noise, we see a sharp peak

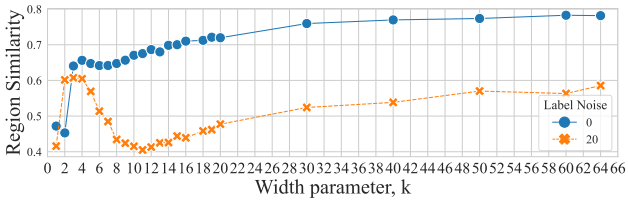

Figure 10. Region similarity scores w.r.t. random initialization for models of different widths. Scores reflect the reproducibility.

in fragmentation score as the model capacity crosses the interpolation threshold, confirming our observations from the visualization in the figures above. Interestingly, this highly sensitive analysis is also able to detect a peak (around $k = 7$) in the fragmentation score for models trained without label noise even though this distinction is hard to spot for a human eye. The bottom part of Fig. 9 quantifies the fragmentation trend for the decision regions spanned by triplets of the same class (like in Fig. 14).

4.3. Quantifying class region stability

Theoretical studies of double descent predict that, for simple linear model classes, model variance spikes near the interpolation threshold as decision regions become highly unstable with respect to noise in the data sampling process. Using region similarity scores, we observe that the fragmentation of neural decision boundaries at the interpolation threshold is associated with high variance and model instability. Fig. 10 shows region similarity scores across model capacities with and without label noise. We see that reproducibility across training runs is high in the under- and over-parameterized regimes, but breaks down at the interpolation threshold. Interestingly, our quantifications are sensitive enough to detect a dip in reproducibility even without label noise (around $k = 7$), although the variance introduced by this effect is not strong enough to cause double descent. Note that the model variance in Fig. 10 is caused by differences in random initialization. Classical convex learning theory studies variance with respect to random data sampling. We find that a similar curve is produced by freezing initialization and randomizing the sampling process (see Appendix Fig. 18).

For no label noise case, we see a fragmentation peak (Fig. 9) and we see a region similarity score dip (Fig. 10) around $k = 7$. Hence we hypothesize that $k = 7$ is potentially the interpolation threshold in this scenario.

4.4. Why does label noise amplify double descent?

The dramatic effect of label noise near the interpolation threshold could be caused by two factors: (i) the necessary regions of incorrect class labels that must emerge around mislabeled points for the model to interpolate them, or (ii) instability in the class boundaries, resulting in oscillations that are not needed to interpolate the data. Quantitative evidence presented above suggests that (ii) is the predominant mechanism of double descent. The lower fragmentation scores in over-parameterized regime (where almost all mislabeled points are interpolated) compared to critical regime as seen in Fig. 9 shows that the extra regions are not needed for interpolation.

To lend more strength to this conclusion, we investigate hypothesis (i) by measuring the "mean margin," which we define to be the average distance between an image and the edge of its class region in a random direction. For each image, we approximate this value using a bisection search in 10 random directions. We compute the mean margin for 5000 data points and report the median for models with and without label noise in Appendix Fig. 15.

Both with and without label noise, the margins are increasing for $k \geq 10$ (the over-parameterized regime). The interesting observation is, when we computed margins of only the mislabeled points, they go up too! The fact that test error descends, even as the regions around mislabeled points grow, lends further strength to the notion that double descent is predominantly driven by the "unnecessary" oscillations resulting from model instability, and not by the error bubbles around mislabeled points.

5. Conclusion

In this article, we use visualizations and quantitative methods to investigate model reproducibility, inductive bias, and double descent from an empirical/scientific perspective. These explorations reveal several interesting behaviors of neural models that we do not think have been previously observed. Curiously, the results of Section 3 indicate that different model families achieve low test error by different inductive strategies; While ResNet-18 and ViT make similar predictions on test data, there are dramatic differences in the decision boundaries they draw. Also, while our studies of double descent found that the model instability predicted for linear models is also observed for neural networks, we saw that this instability is manifested as the dramatic fragmentation of class regions. This instability involves the emergence of many small "bubbles" of incorrect class regions, and is unique to the non-convex setting.

6. Acknowledgements

This work was supported by the ONR MURI program, the Office of Naval Research, the National Science Foundation (DMS-1912866), and DARPA GARD (HR00112020007). Additional funding was provided by Capital One Bank and Kulkarni Summer Research Fellowship.

References

[1] Ben Adlam and Jeffrey Pennington. Understanding double descent requires a fine-grained bias-variance decomposition. *arXiv preprint arXiv:2011.03321*, 2020. 5

[2] Madhu S Advani, Andrew M Saxe, and Haim Sompolinsky. High-dimensional dynamics of generalization error in neural networks. *Neural Networks*, 132:428–446, 2020. 5

[3] Anonymous. Decision boundary variability and generalization in neural networks. In *Submitted to The Tenth International Conference on Learning Representations*, 2022. under review. 4

[4] Mikhail Belkin, Daniel Hsu, Siyuan Ma, and Soumik Mandal. Reconciling modern machine-learning practice and the classical bias–variance trade-off. *Proceedings of the National Academy of Sciences*, 116(32):15849–15854, 2019. 5

[5] Pratik Chaudhari, Anna Choromanska, Stefano Soatto, Yann LeCun, Carlo Baldassi, Christian Borgs, Jennifer Chayes, Levent Sagun, and Riccardo Zecchina. Entropy-sgd: Biasing gradient descent into wide valleys. *Journal of Statistical Mechanics: Theory and Experiment*, 2019(12):124018, 2019. 1

[6] Yehuda Dar, Vidya Muthukumar, and Richard G Baraniuk. A farewell to the bias-variance tradeoff? an overview of the theory of overparameterized machine learning. *arXiv preprint arXiv:2109.02355*, 2021. 5

[7] Jia Deng, Wei Dong, Richard Socher, Li-Jia Li, Kai Li, and Li Fei-Fei. Imagenet: A large-scale hierarchical image database. In *2009 IEEE conference on computer vision and pattern recognition*, pages 248–255. Ieee, 2009. 3

[8] Laurent Dinh, Razvan Pascanu, Samy Bengio, and Yoshua Bengio. Sharp minima can generalize for deep nets. In *International Conference on Machine Learning*, pages 1019–1028. PMLR, 2017. 1

[9] Alexey Dosovitskiy, Lucas Beyer, Alexander Kolesnikov, Dirk Weissenborn, Xiaohua Zhai, Thomas Unterthiner, Mostafa Dehghani, Matthias Minderer, Georg Heigold, Sylvain Gelly, et al. An image is worth 16x16 words: Transformers for image recognition at scale. *arXiv preprint arXiv:2010.11929*, 2020. 3

[10] Stéphane d'Ascoli, Maria Refinetti, Giulio Biroli, and Florent Krzakala. Double trouble in double descent: Bias and variance (s) in the lazy regime. In *International Conference on Machine Learning*, pages 2280–2290. PMLR, 2020. 5

[11] Alhussein Fawzi, Seyed-Mohsen Moosavi-Dezfooli, Pascal Frossard, and Stefano Soatto. Empirical study of the topology and geometry of deep networks. In *Proceedings of the IEEE Conference on Computer Vision and Pattern Recognition*, pages 3762–3770, 2018. 2, 7

[12] Pierre Foret, Ariel Kleiner, Hossein Mobahi, and Behnam Neyshabur. Sharpness-aware minimization for efficiently improving generalization. *arXiv preprint arXiv:2010.01412*, 2020. 3, 5

[13] Jonas Geiping, Micah Goldblum, Phillip E Pope, Michael Moeller, and Tom Goldstein. Stochastic training is not necessary for generalization. *arXiv preprint arXiv:2109.14119*, 2021. 4

[14] Stuart Geman, Elie Bienenstock, and René Doursat. Neural networks and the bias/variance dilemma. *Neural computation*, 4(1):1–58, 1992. 5

[15] Micah Goldblum, Liam Fowl, Soheil Feizi, and Tom Goldstein. Adversarially robust distillation. In *Proceedings of the AAAI Conference on Artificial Intelligence*, volume 34, pages 3996–4003, 2020. 4

[16] Trevor Hastie, Andrea Montanari, Saharon Rosset, and Ryan J Tibshirani. Surprises in high-dimensional ridgeless least squares interpolation. *arXiv preprint arXiv:1903.08560*, 2019. 5

[17] Kaiming He, Xiangyu Zhang, Shaoqing Ren, and Jian Sun. Deep residual learning for image recognition. In *Proceedings of the IEEE conference on computer vision and pattern recognition*, pages 770–778, 2016. 3, 5

[18] Warren He, Bo Li, and Dawn Song. Decision boundary analysis of adversarial examples. In *International Conference on Learning Representations*, 2018. 2

[19] Geoffrey Hinton, Oriol Vinyals, and Jeff Dean. Distilling the knowledge in a neural network. *arXiv preprint arXiv:1503.02531*, 2015. 4

[20] Gao Huang, Zhuang Liu, Laurens Van Der Maaten, and Kilian Q Weinberger. Densely connected convolutional networks. In *Proceedings of the IEEE conference on computer vision and pattern recognition*, pages 4700–4708, 2017. 3

[21] Hamid Karimi, Tyler Derr, and Jiliang Tang. Characterizing the decision boundary of deep neural networks. *arXiv preprint arXiv:1912.11460*, 2019. 2

[22] Diederik P Kingma and Jimmy Ba. Adam: A method for stochastic optimization. *arXiv preprint arXiv:1412.6980*, 2014. 3

[23] Alex Krizhevsky, Geoffrey Hinton, et al. Learning multiple layers of features from tiny images. 2009. 2

[24] Michel Ledoux. *The concentration of measure phenomenon*. Number 89. American Mathematical Soc., 2001. 2, 1

[25] Hao Li, Zheng Xu, Gavin Taylor, Christoph Studer, and Tom Goldstein. Visualizing the loss landscape of neural nets. *arXiv preprint arXiv:1712.09913*, 2017. 1

[26] Vidya Muthukumar, Kailas Vodrahalli, Vignesh Subramanian, and Anant Sahai. Harmless interpolation of noisy data in regression. *IEEE Journal on Selected Areas in Information Theory*, 1(1):67–83, 2020. 5

[27] Preetum Nakkiran, Gal Kaplun, Yamini Bansal, Tristan Yang, Boaz Barak, and Ilya Sutskever. Deep double descent: Where bigger models and more data hurt. *arXiv preprint arXiv:1912.02292*, 2019. 5, 6

[28] Brady Neal, Sarthak Mittal, Aristide Baratin, Vinayak Tantia, Matthew Scicluna, Simon Lacoste-Julien, and Ioannis Mitliagkas. A modern take on the bias-variance tradeoff in neural networks. *arXiv preprint arXiv:1810.08591*, 2018. 5

[29] Manfred Opper. Statistical mechanics of learning: Generalization. *The handbook of brain theory and neural networks*, pages 922–925, 1995. 5

[30] Manfred Opper. Learning to generalize. *Frontiers of Life*, 3(part 2):763–775, 2001. 5

[31] Ali Shafahi, W Ronny Huang, Christoph Studer, Soheil Feizi, and Tom Goldstein. Are adversarial examples inevitable? *arXiv preprint arXiv:1809.02104*, 2018. 2, 1

[32] Karen Simonyan and Andrew Zisserman. Very deep convolutional networks for large-scale image recognition. *arXiv preprint arXiv:1409.1556*, 2014. 3

[33] Stefano Spigler, Mario Geiger, Stéphane d'Ascoli, Levent Sagun, Giulio Biroli, and Matthieu Wyart. A jamming transition from under-to over-parametrization affects loss landscape and generalization. *arXiv preprint arXiv:1810.09665*, 2018. 5

[34] Samuel Stanton, Pavel Izmailov, Polina Kirichenko, Alexander A Alemi, and Andrew Gordon Wilson. Does knowledge distillation really work? *arXiv preprint arXiv:2106.05945*, 2021. 4

[35] Ilya Tolstikhin, Neil Houlsby, Alexander Kolesnikov, Lucas Beyer, Xiaohua Zhai, Thomas Unterthiner, Jessica Yung, Andreas Steiner, Daniel Keysers, Jakob Uszkoreit, et al. Mlp-mixer: An all-mlp architecture for vision. *arXiv preprint arXiv:2105.01601*, 2021. 3

[36] Ross Wightman. Pytorch image models. `https://github.com/rwightman/pytorch-image-models`, 2019. 3

[37] Zitong Yang, Yaodong Yu, Chong You, Jacob Steinhardt, and Yi Ma. Rethinking bias-variance trade-off for generalization of neural networks. In *International Conference on Machine Learning*, pages 10767–10777. PMLR, 2020. 5

[38] Sergey Zagoruyko and Nikos Komodakis. Wide residual networks. *arXiv preprint arXiv:1605.07146*, 2016. 3

[39] Chiyuan Zhang, Samy Bengio, Moritz Hardt, Benjamin Recht, and Oriol Vinyals. Understanding deep learning (still) requires rethinking generalization. *Communications of the ACM*, 64(3):107–115, 2021. 3

[40] Hongyi Zhang, Moustapha Cisse, Yann N Dauphin, and David Lopez-Paz. mixup: Beyond empirical risk minimization. *arXiv preprint arXiv:1710.09412*, 2017. 2